Biomedical Microdevices (2021) 23:45
https://doi.org/10.1007/s10544-021-00579-8

A portable multi-sensor module for monitoring external ventricular drains

Trevor Q. Hudson[1] · Alex Baldwin[1] · Aria Samiei[2] · Priya Lee[1] · J. Gordon McComb[3] · Ellis Meng[1,2]

Accepted: 20 August 2021

Abstract

External ventricular drains (EVDs) are used clinically to relieve excess fluid pressure in the brain. However, EVD outflow rate is highly variable and typical clinical flow tracking methods are manual and low resolution. To address this problem, we present an integrated multi-sensor module (IMSM) containing flow, temperature, and electrode/substrate integrity sensors to monitor the flow dynamics of cerebrospinal fluid (CSF) drainage through an EVD. The impedimetric sensors were microfabricated out of biocompatible polymer thin films, enabling seamless integration with the fluid drainage path due to their low profile. A custom measurement circuit enabled automated and portable sensor operation and data collection in the clinic. System performance was verified using real human CSF in a benchtop EVD model. Impedimetric flow sensors tracked flow rate through ambient temperature variation and biomimetic pulsatile flow, reducing error compared with previous work by a factor of 6.6. Detection of sensor breakdown using novel substrate and electrode integrity sensors was verified through soak testing and immersion in bovine serum albumin (BSA). Finally, the IMSM and measurement circuit were tested for 53 days with an RMS error of 61.4 µL/min.

Keywords Flow sensor · External ventricular drain · Parylene C · Electrochemical impedance · Cerebrospinal fluid (CSF) · MEMS

1 Introduction

An external ventricular drain (EVD) is a device commonly used in neurosurgery to relieve raised intracranial pressure (ICP) secondary to a disturbance in cerebrospinal fluid (CSF) circulation resulting from obstruction by tumors, cysts, bleeding, infection, and trauma (Drake et al. 1991). The placement of an EVD involves incising the scalp, drilling a hole through the skull, perforating the covering of the brain (dura mater) and inserting a catheter into the CSF-filled cavities (ventricles) within the brain (Muralidharan 2015). This catheter is attached to a CSF-collecting bag at a pressure that can be regulated by varying the height of the drainage tubing. The EVD is kept in place anywhere from 1 to 28 days (7–15 on average) (Kirmani et al. 2015; Lackner et al. 2008; Roitberg et al. 2001). If the ICP remains chronically elevated, a condition known as hydrocephalus, then a permanent indwelling shunt must be installed afterwards which diverts CSF drainage elsewhere in the body, typically the abdomen (Rammos et al. 2008).

EVD settings must be closely monitored to avoid overdrainage and underdrainage of CSF, which can cause slit ventricle syndrome, subdural hematoma, and other conditions (Gardner et al. 2009). Such manual monitoring is somewhat qualitative and increases nursing workload. Moreover, internal factors such as crying, laughing, sneezing, respiration, etc. and external factors such as head and body position and the variable set height of the drainage system can affect CSF flow rate minute to minute (Kadowaki et al. 1995). The gold standard for monitoring the effectiveness of EVD treatment is direct measurement of ICP through an attached pressure sensor (Czosnyka and

✉ Ellis Meng
ellis.meng@usc.edu

[1] Department of Biomedical Engineering, University of Southern California, 1042 Downey Way, Los Angeles, CA 90089, USA

[2] Ming Hsieh Department of Electrical and Computer Engineering, University of Southern California, 3740 McClintock Avenue, Los Angeles, CA 90089, USA

[3] Division of Neurosurgery, Children's Hospital Los Angeles, 1300 N. Vermont Ave. Suite 1006, Los Angeles, CA 90027, USA

Published online: 20 September 2021

Pickard 2004). For such measurements, the zero-pressure mark of the pressure transducer must be precisely aligned vertically to the ear; placement above or below this point would result in positive or negative ICP measurement error, respectively. The drainage flow rate of CSF is then adjusted by raising or lowering the collection bag to tune the hydrostatic pressure difference between the implanted ventricle and collection bag. The only method used in clinic to monitor flow rate involves manually recording accumulated CSF volume in the attached collection bag at hourly intervals. Total CSF drainage is usually in the range of 100–500 mL in a 24 h period (69–347 μL/min).

Wireless devices for monitoring ICP in EVDs have been proposed and are currently being investigated (Limbrick et al. 2012). Flow sensors for monitoring CSF outflow in EVDs and implanted shunts have been reported. Apigo et al. developed a differential, membrane-based capacitive sensor capable of measuring pressure and flow rates and fabricated using silicon micromachining (Raj et al. 2015; Apigo et al. 2016; 2017). Krishnan et al. built a transcutaneous thermal flow sensor on a polyimide and silicone wearable patch able to distinguish between three flow levels (Krishnan et al. 2018). Clark et al. measured pressure from a membrane-integrated piezoresistor pair, then repurposed the same resistors to measure flow by exploiting their self-heating and thermal sensitivity properties (Clark et al. 2015). Qin et al. published an inline shunt flow sensor using a single thermistor as an anemometer (Qin et al. 2019). Enikov et al. proposed a copper and chromium cantilever placed upright in the shunt lumen such that increased flow rate resulted in increased deformation (Enikov et al. 2015). A commercial device, ShuntCheck, infers flow using a thermal tracer provided by an ice block placed across the skin over the drainage catheter and picked up by downstream thermistors (Madsen et al. 2020).

Applications for such sensors include electronic monitoring of EVD outflow rates with alarms to indicate any abnormalities (Lutz et al. 2013). Flow sensors may be combined with a control algorithm and actuator to achieve a closed loop EVD (Misgeld et al. 2015; Krause et al. 2011). A fully implanted closed loop smart shunt would revolutionize hydrocephalus care by reducing diagnostic ambiguity and surgical intervention.

However, most microfabricated sensors are designed using stiff substrates such as silicon. While processing techniques for silicon are well-established, there are significant challenges for implementing the material in vivo, including susceptibility to corrosion, need for hermetic packaging or passivation, provocation of the inflammatory response, and risk of fracture (Hämmerle et al. 2002; Wang et al. 2007; Scholten and Meng 2015). Sensors fabricated on biocompatible polymer substrates can offer improved performance and lifetime in vivo.

In this work, a flow sensor (Hudson et al. 2019) is supported by several sensors which monitor device performance in a compact, freestanding thin-film device, dramatically improving its practical utility. Such a device may enable more accurate implanted valve pressure adjustment and the inference of shunt occlusion via sustained periods of low flow. Compared with previous work, here the flow sensor is accompanied by a resistance temperature detector (RTD) and temperature compensation algorithm to reduce error by a factor of 6.6 while also providing body temperature data. In addition, in vivo performance degradations caused by crosstalk and electrode fouling can be tracked using a novel electrode/substrate integrity sensor based on impedance differences between exposed and passivated interdigitated electrode pairs. This sensor monitors device health and therefore assists in the interpretation of collected flow and temperature data.

Instead of adapting existing sensors for in vivo use, each sensor here is purposefully designed for use in the body and in the presence of its saline environment. Electrochemical impedance-based flow sensing repurposes local CSF as a temperature sensor and thermal anemometer. This approach removes the need for a passivation layer over the sensor, improving sensitivity and thus lowering the overheat temperature at which the sensor operates The electrode/substrate integrity sensor is also impedimetric, simplifying data acquisition. Sensor construction using Parylene C improves thermal isolation because of the material's low thermal conductivity and its low Young's modulus also reduces the mechanical mismatch between tissue and substrate when compared against silicon (Wang et al. 2007; Moshayedi et al. 2014).

To enable practical implementation on a clinical EVD, a portable, low-power electronic measurement system was designed to automatically operate and record data from the sensors, collectively referred to as the integrated multisensor module (IMSM) (Fig. 1). Benchtop experiments characterizing the IMSM using saline solution and human CSF are reported. For the first time, long-term performance of the IMSM and circuit was also evaluated over approximately 2 months in an in vitro EVD model.

2 Sensor design

The IMSM integrates multiple independent sensors which measure impedance to transduce flow rate, temperature, and electrode/substrate integrity. Electrochemical impedance is a measure of the obstruction that current experiences as it is converted from electronic to ionic flow across the electrode–electrolyte interface, passes through solution, then returns through the electrode into the measurement circuit. Impedance measurement is relatively simple to implement

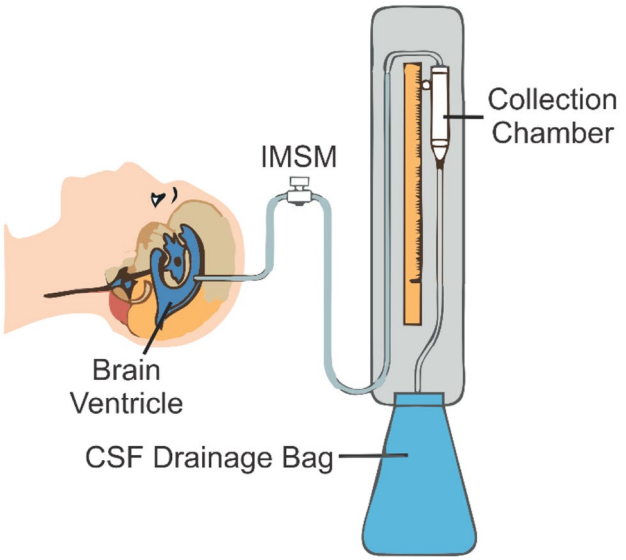

Fig. 1 Schematic of IMSM attached to EVD. The collection chamber is adjusted to a known height above the ventricles to regulate ICP

and can transduce an array of quantities with appropriate sensor geometry and interrogation timing (Fig. 2).

2.1 Flow sensor

The flow sensor consists of an insulated, serpentine resistive trace which creates a thermal tracer in the adjacent flow via Joule heating, and one pair of exposed impedimetric electrodes located downstream to detect the injected tracer (Baldwin et al. 2016). By elevating the interrogation frequency of the impedance measurement, the contribution of the electrode–electrolyte interface is minimized and solution resistance, which is temperature-sensitive, can be measured with high fidelity at the downstream electrodes (Baldwin et al. 2019). All measurements here are taken at 50 kHz to balance power consumption and parasitic signal loss through packaging.

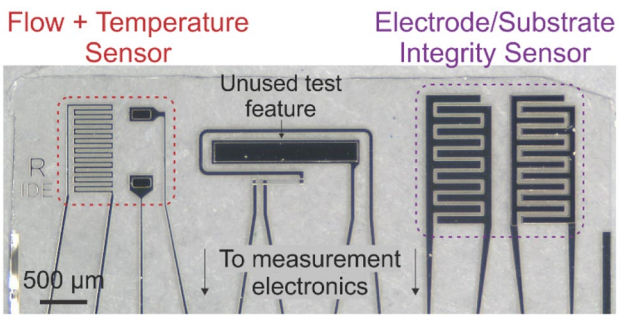

Fig. 2 Micrograph of sensor die. The combined dimensions of the sensors in this work are 2660 × 1400 µm

Conduction and convection transfer the thermal signal downstream when fluid flow is present. The heater is driven with 10 s constant voltage pulses to minimize overheat temperature (~ 1.6 °C) and power consumption. At the exposed electrodes, the heating pulse results in a temperature increase which in turn registers as a decrease in impedance (Z; Fig. 3a). The rate of change of impedance with respect to time, $\frac{dZ}{dt}$, during heating can then be used to transduce flow rate Q (Fig. 3b) (Baldwin et al. 2016). Flow can be measured once per 80 s, limited by a cooldown period between pulses.

2.2 Temperature sensor

While impedimetric flow sensing possesses high sensitivity $S = \frac{dZ}{dQ}$, S is also dependent on ambient temperature T. Depending on the temperature and flow rate range, impedance-normalized $\frac{dS}{dT}$ is as high as 3%/°C. For applications involving a range of potential temperatures, additional calibration incorporating temperature is essential (see section V).

The sensorized EVD, our target application, measures CSF flow in the drainage path just outside the body. Due

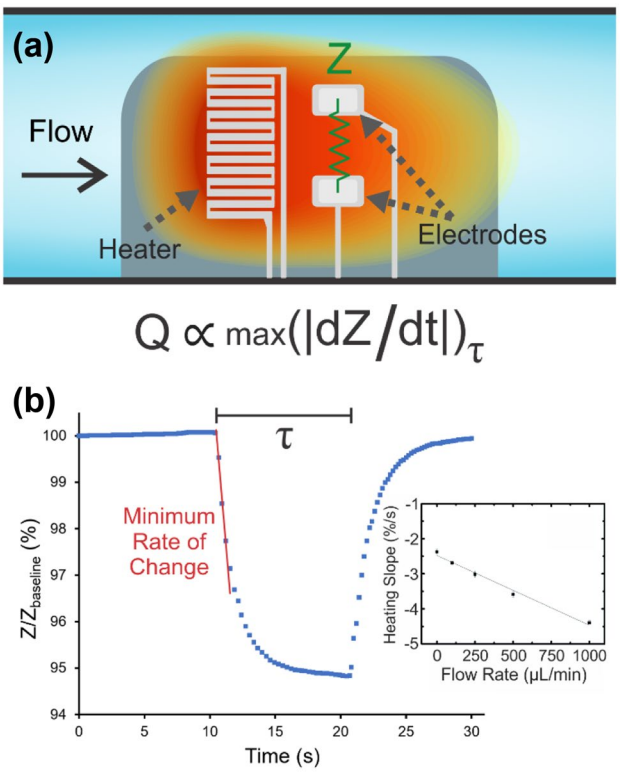

Fig. 3 **a** Illustration showing local fluid temperature of the flow sensor during the heater activation period τ. **b** Impedance response over a typical heating cycle. The normalized minimum rate of change of impedance is used to transduce flow rate. Inset shows a typical calibration curve

to variables such as the length of drainage line between the sensor and body exit point, CSF flow rate, and ambient air temperature in the clinic, the CSF temperature can vary from 20–37 °C, covering a significant range of sensitivities. Some preliminary measurements recorded in the laboratory are given in Table 1. Thus, temperature tracking and calibration is necessary for EVD flow monitoring. Body temperature ranges from 30 – 37 °C depending on air temperature and interpersonal variation (Webb 1992), which may be important for operation of sensors in implanted shunt systems where the likely site for sensor integration is just below the skin. Body temperature tracking may also provide additional information, such as in the diagnosis of fever which can indicate infection, a common mechanism of shunt failure (Hanak et al. 2017).

Impedimetric temperature sensing can suffer from drift in chronic biologic applications due to changes in solute ionic strength and electrode/substrate integrity, and thus is best suited for transient measurement unless additional drift-resistant features are incorporated (Hudson et al. 2019). As a redundant measure, a low-side current measurement circuit was added using the serpentine heater trace (Fig. S1) as an RTD element to measure ambient fluid temperature. Briefly, the temperature coefficient of resistance of platinum enables transduction via a low-side current sensing circuit, which measures the voltage across a small-valued shunt resistor (1 Ω) in-line with the load (~480 Ω). Temperature is transduced at the start of the heating period before appreciable self-heating of the serpentine trace occurs. This additional temperature sensor greatly improves flow sensor performance and monitors patient internal temperature with a minimal increase in complexity or power consumption.

2.3 Electrode/substrate integrity sensors

Thin-film, multilayer, polymer and metal devices are susceptible to different failure modes over time (Ortigoza-Diaz et al. 2018). Despite Parylene's low water vapor transmission (0.4 g·mm/(m^2·day)) and water absorption rates, bulk water absorption may result in water accumulation between nominally adhered polymer and metal layers and may lead to gradual film delamination. Gradual and undesirable changes in sensor performance may result; partial metal delamination may cause higher effective surface area, lower electrode impedance, electrical crosstalk, and parasitic impedances between signals on adjacent metal traces.

Biofouling, or the accumulation of unwanted biological matter on surfaces, may lead to device failure. While CSF has relatively low protein and cell counts (Di Terlizzi and Platt 2006), proteins such as albumin and fibrinogen absorb to polymer surfaces just seconds after contact (Cottonaro et al. 1981) and can stimulate the adhesion and proliferation of astrocytic tissue ingrowth leading to shunt occlusion, as well as instigate further damaging immune responses (Del Bigio and R 1998; Tracey L. Bonfield et al. 1989; T. L. Bonfield et al. 1992). Progenitors of tissue encapsulation like fibroblasts and glial cells also proliferate on platinum (Pennisi et al. 2009; Turner et al. 2004), which can degrade signal quality of implanted devices. Bacterial or fungal growth on shunt hardware also affects 3–20% of implanted shunts, one of the most urgent complications which typically requires full shunt replacement (Prusseit et al. 2009; Turgut et al. 2005).

Label-free, rapid detection of biofouling is an area of ongoing research (Yang and Li 2006; Gomez-Sjoberg et al. 2005); notably, Kim et al. demonstrated that EIS between exposed electrodes can be used to measure bacterial biofouling (S. Kim et al. 2012). Strong platinum adsorption of bovine serum albumin (BSA), an analogue of the most common human blood protein, is detectable using cyclic voltammetry (Cosman and Roscoe 2004; Rouhana et al. 1997). Spectral data on albumin adsorption to platinum is rare, though EIS adsorption data is available with different metals, such as BSA on stainless steel (Omanovic and Roscoe 1999), and different proteins, such as yeast alcohol dehydrogenase (Phillips et al. 2001) and L-phenylalanine (Wright et al. 2003) on platinum.

To monitor device health in situ, electrode and substrate integrity sensors were integrated consisting of two interdigitated electrodes (IDE) pairs. The IDE pairs are of identical size and shape, with one covered in Parylene and one exposed to solution (Fig. 4). Based on this geometry, the differential impedance between each pair should measure only exposed electrode effects, while the impedance of the covered pair should measure changes in the substrate. Practically, electrode behavior can be analyzed with the exposed IDE pair alone since the impedance contribution of the covered pair is 2–3 orders of magnitude higher and in parallel and so can be ignored.

Table 1 Fluid temperature versus distance from brain phantom at 37 °C and 330 µL/min

Tubing length (cm)	Fluid temperature (°C)
5	34.0
10	29.1
15	27.1

2.4 Fabrication and packaging

Sensor fabrication follows established micromachining processes for Parylene C (B. J. Kim and Meng 2016). First, 10 µm of Parylene C was deposited onto a silicon carrier wafer at 35 mtorr using the Gorham process (Labcoter 2, Specialty Coating Systems, Indianapolis, IN) (Gorham

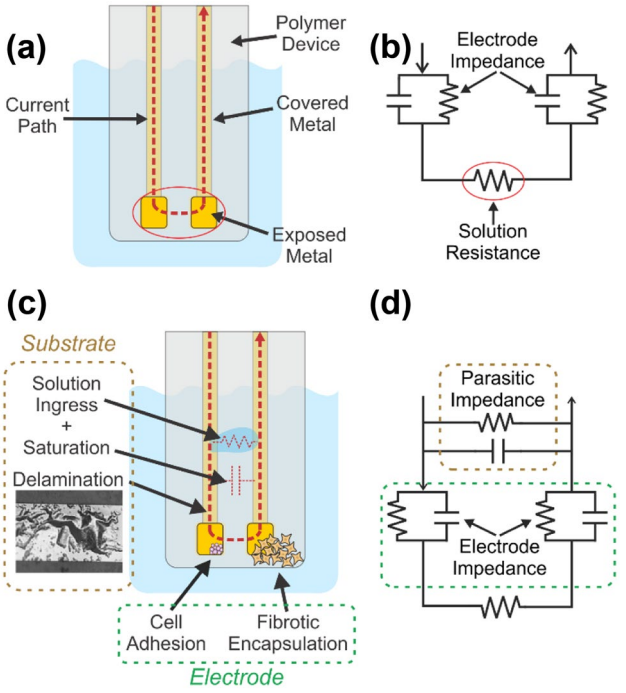

Fig. 4 **a** Diagram of idealized polymer impedimetric device. **b** Randles circuit model of same. **c** Diagram of failures which develop after implantation. **d** Randles circuit model with adjustments for in situ failure modes

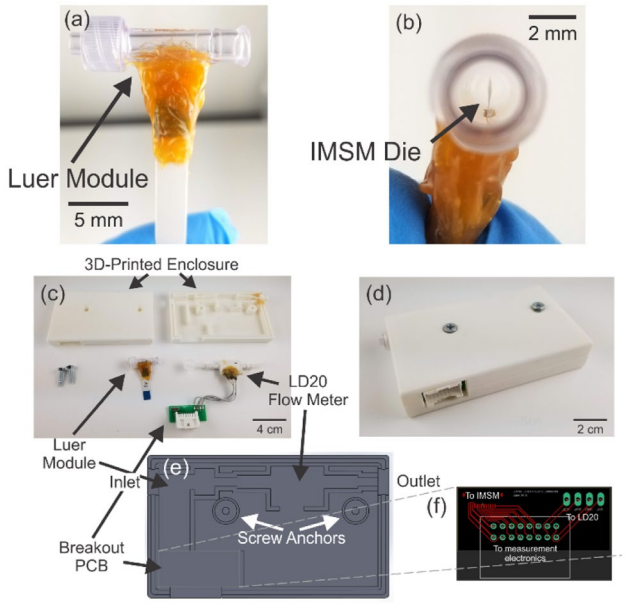

Fig. 5 **a** Photograph of sensor in Luer module. **b** The freestanding polymer sensor is packaged in the center of the module. **c** View of sensor enclosure components including 3D printed case, packaged IMSM, LD20 flow sensor, and sensor enclosure breakout board. **d** Fully assembled sensor enclosure. **e** IMSM sensor enclosure schematic. Top down view of box bottom. Devices were connected with silicone tubing. **f** Breakout PCB layout

1966). Sensor features and contact pads were defined using a lift-off procedure by electron-beam-deposition of 2000 Å of platinum (International Advanced Materials, North Charleston, SC) onto patterned AZ 5214 photoresist (1.6 µm; Merck KGaA, Darmstadt, DE). A second 10 µm layer of Parylene C was deposited as an insulation layer. Then, electrodes and contact pads were exposed using a Bosch process-like oxygen-based deep reactive ion etch with AZ 4620 (10 µm; Merck KGaA, Darmstadt, DE) photoresist as an etch mask (Meng et al. 2008). Devices were released from the carrier silicon wafer (University Wafer, Boston, MA) by gently peeling while submerged in deionized water. Finally, devices were annealed at 200 °C for 48 h under vacuum to increase adhesion between Parylene layers, reduce risk of delamination, and improve barrier properties (Rodger et al. 2008).

Sensor packaging involved placing and sealing the sensor into its flow chamber, electrically connecting its contact pads to measurement circuitry, and insulating sensor electronics from the fluid under test. To enable electrical contact, a ~ 180 µm (7 mil) thick polyetheretherketone backing was attached to the reverse side of the contact pad region to provide rigidity, allowing devices to be locked in a flip-lock zero insertion force connector in a solder-less packaging scheme (Gutierrez et al. 2011). Sensors were inserted into Luer-compatible modules (ID 3.25 mm; 80,379, Qosina, Edgewood, NY) through 0.56×8 mm^2 machined slits which allowed for easy integration into catheter systems currently used in the clinic (Fig. 5a, b). Biocompatible epoxy (EpoTek 353 ND-T, Epoxy Technology, Inc., Billerica, MA) was then used to pot contact pads and fluidically seal the sensor in the Luer module.

3 Electronics design

3.1 System overview

A custom electronic datalogger was built for automated impedance measurement in the clinic. The main goals for the circuit were to measure impedance between the three sensor electrode pairs and to energize the flow sensor heater. The measurement circuit was placed in an ABS plastic enclosure measuring $9.5 \times 7.7 \times 3.0$ cm^3 (62.13 g) (1593BB, Hammond Mfg. Ltd., Guelph, Ontario) to protect the electronics from damage or short circuits caused by splashed fluid (Fig. S2).

To maintain device performance during storage, the circuit was designed with a shelf life of up to 6 months without requiring swapping or recharging of the battery. The circuit had to be easily operable by clinical personnel with no engineering experience and little knowledge of our study. To meet these constraints, the circuit was activated by clinical personnel via a simple SPST switch on the enclosure and

associated with a single, adjacent red LED, indicating the circuit was powered. The circuit was activated only once after the sensors were connected to the patient's drainage line – no further user input was needed.

Each sensor was queried sequentially each hour to mimic typical clinical protocol (Fig. S3). Three flow sensor readings were recorded in a row, then averaged to provide a final output and standard deviation. Next, the electrode/substrate integrity sensor was interrogated to complete one full measurement cycle. The measurement circuit connected to the sensor die via a multi-channel cable and data was stored locally on a microSD card. Between cycles, the circuit was placed into a quiescent "sleep" mode, in which microcontroller clock speed was set to the lowest possible value, all I/O ports were set to a high impedance state, and all discrete IC components were powered off.

3.2 Electronics implementation

Impedance was measured via a network analyzer (AD5933, Analog Devices, Norwood, MA; Fig. S4), a popular choice for portable impedance measurement (A. Al-Ali et al. 2017; A. A. Al-Ali et al. 2019; Rasalingam 2018; Nordbotten 2008). Without modification, the AD5933 has a measurement range of 1 kΩ to 10 MΩ at frequencies of 1 to 100 kHz. The maximum perturbation signal amplitude was used (2.0 V_{P-P}) to increase signal strength. An analog front-end circuit was added in series with the transmit and receive stages to improve device performance (Analog Devices 2005) (Fig. S5). The signal was filtered through a capacitor, then rebiased to $V_{supply}/2$ in order to match the receive stage. After, the signal was buffered to reduce output impedance (AD8606, Analog Devices), which ranged from 200 to 2400 Ω depending on the chosen signal amplitude with no buffer. The signal was routed to one of three electrode pairs through a differential four channel multiplexer (ADG709, Analog Devices). After passing through the device under test, the signal was routed through an external transimpedance amplifier (TIA) (AD8606, Analog Devices) for its lower leakage current and noise compared to the internal TIA.

A Teensy 3.2 USB development board (PJRC, LLC, Sherwood, OR) provided sensor control, measurement timing, and data processing. The Teensy 3.2 contains a MK20DX256 microcontroller (Freescale Semiconductor, Austin, TX), which uses a 72 MHz ARM processor, contains two 16-bit ADCs and one 12-bit DAC, and 34 I/O pins. A digital DC output was applied from an I/O pin to the flow sensor heater. Data was stored locally via SPI communication with a micro SD card adaptor. A 2000 mAh LiPo battery with a nominal voltage of 3.7 V (DTP 605,068, Sparkfun Electronics, Boulder, CO) powered the Teensy board, which then supplied the remainder of the circuit with a stable 3.3 V rail. The battery was stored under the circuit board in the plastic enclosure.

3.3 Integrated commercial flow sensor

A lightweight commercial flow sensor (LD20-2600B, Sensirion AG, ZH, Switzerland) was used to directly measure CSF flow rate simultaneously with our impedimetric measurements and provide a redundant flow measurement as a benchmark. The LD20 is marketed as a single-use flow sensor and designed for compact and cost-effective performance. It can measure flow rates up to 1000 mL/h, which is sufficient for neonatal CSF monitoring. The LD20 is a thermal flow sensor with low overheat temperature of < 3 °C, uses only polymeric wetted materials, and as such, is intended for biomedical applications. Electrical connection was achieved by soldering wires directly to the LD20's contact pads then potting using 353ND-T epoxy. The LD20 and IMSM were held in a 3D-printed enclosure for protection (Fig. 5c-f). The LD20 is intended to assess impedimetric flow sensor performance and is not intended to be part of a standalone implanted sensor.

In preparation for using the LD20 in the clinic, we tested the sensor response following H_2O_2 plasma sterilization, which is required for all equipment which will contact circulating CSF in the hospital. There was no detectable performance change to the sensor based on calibration curves taken before and after sterilization (Fig. S6). Our previous work showed that H_2O_2 plasma sterilization did not affect exposed platinum electrodes (Kim et al. 2016).

4 In vitro testing methods

4.1 Benchtop EVD model

Sensors were characterized in vitro using a benchtop EVD model (Fig. 6). The brain was modeled using a sealed graduated glass bottle containing fluid housed in an oven (EC0A, Sun Electronic Systems, Titusville, FL) and maintained at 37 °C. The fluid was pumped to a sealed collection bottle outside the enclosure using a pressure-controlled pneumatic pump capable of providing precise feedback-controlled flow rate (Flow EZ, Fluigent, Paris, FR); before testing, flow rate was validated gravimetrically. Flow testing was performed using both 1 × phosphate-buffered saline (PBS) and deidentified human CSF collected from EVDs and frozen until use (with approval from the Children's Hospital Los Angeles IRB, CHLA-14–00,332). The IMSM was placed ~ 1 cm from the oven to mimic its use in a clinical EVD, except during flow rate calibration when it was kept in the oven. The measurement electronics were kept outside the oven in both cases.

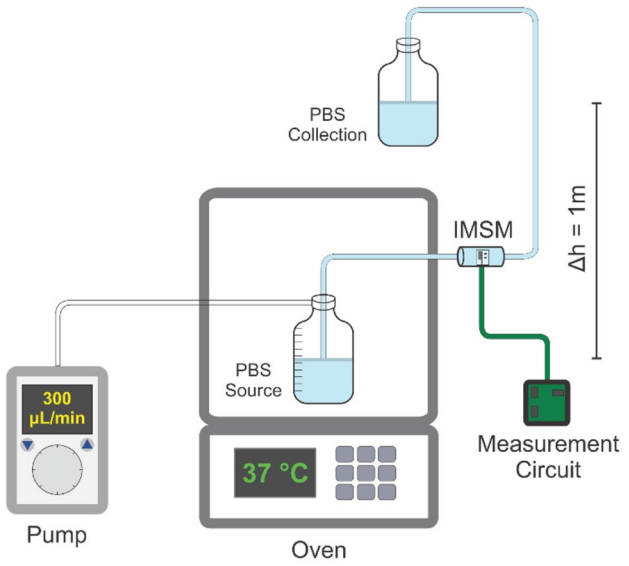

Fig. 6 Diagram of experimental setup for chronic experiments. Flow was pumped upwards, then allowed to drain back into the source beaker to enable automatic testing. For calibration, the IMSM was placed inside the oven

For chronic measurements, the collection bottle was held at ~ 1 m above the source bottle. Flow was alternately pumped upwards then allowed to drain back into the source bottle to refill it; flow control and automation utilized LabVIEW and Python. Pumping was synchronized to the hour-long measurement period of the IMSM so that only source-to-collection flow data was recorded. A physiologically-recorded ICP data set which incorporates cardiac and respiratory pulsatility was used to control the applied pressure (Czosnyka and Pickard 2004). The ICP data set was translated to a higher pressure to offset the increased hydrostatic pressure and bring the average flow rate to a physiological value (330 µL/min). The ICP data set was 371 s long and was looped over the test duration. The IMSM was mains-powered for chronic testing.

4.2 Soak testing

In soak testing experiments, devices were interfaced with glass vials containing 1 × PBS by passing though a slit milled through the corresponding polypropylene caps and secured (353 ND-T epoxy) while allowing for an external cable connection. The vials were sealed to minimize evaporative conductivity change and soaked in a hot water bath (2864, Thermo Scientific, Waltham, MA) at 37 °C. Electrochemical impedance spectroscopy (EIS) was performed immediately after removing from the water bath at semi-regular intervals. EIS measurements were recorded over the bandwidth of the network analyzer in the datalogger (5 – 95 kHz) at 5 kHz increments. A 1 × or 5 × programmable gain amplifier in the receive stage was used for the exposed and covered electrodes respectively to extend the impedance magnitude measurement range. EIS was also performed using a Reference 600 Potentiostat (Gamry Instruments, Warminster, PA) as a benchmark measurement. The Gamry was operated with a 25 mV perturbation signal and no DC bias over a 1 Hz to 10 MHz bandwidth. All EIS recordings used a two electrode cell composed of the platinum device electrodes.

4.3 Preparation of BSA solutions

For fluorescent imaging experiments, fluorescein-conjugated bovine serum albumin (BSA-FITC, Thermo Scientific, Waltham, MA) was prepared and mildly agitated with a vortex mixer before use. For pure electrochemical experiments, untagged BSA (Fraction V – Standard Grade, Gemini Bio-Products, West Sacramento, CA) was used to enable higher sample size.

5 Results

5.1 Flow sensor

Sensor response curves taken at multiple temperatures revealed significant temperature-dependence which can confound interpretation of results (Fig. 7a). A compensation method was devised incorporating the heater as an RTD to track ambient temperature. Briefly, the sensor was calibrated at several temperatures over the anticipated range. The *y*-intercept and slope of the linear fit of sensor response versus flow rate were then parameterized with RTD output (Fig. S7).

Data acquired using the compensation method was compared with uncompensated data calibrated at 40 °C (Fig. 7b). Flow rate was varied nonmonotonically over the experiment. Ambient temperature was decreased from 40 to 22 °C over 40 trials. A trial consisted of 3 averaged flow sensor measurements, requiring about 4 min. Approximately 30 s elapsed between trials, but additional time was allowed when changing temperature, typically 15–20 min. Compensated data had 6.6 × lower error than uncompensated data in this experiment.

Flow sensor performance is often characterized using constant flow. However, CSF outflow is pulsatile, with significant energy at respiratory and cardiac frequencies (0.4 and 1.78 Hz, respectively) (Pennell et al. 2016; Giménez Á. et al. 2017; Linninger et al. 2007). The pulsatile response of the IMSM was captured by driving a physiological ICP signal (Czosnyka and Pickard 2004) then recording the output flow sensor curves (Fig. 8). The effect of pulse amplitude was tested by multiplying ICP amplitude by various integers.

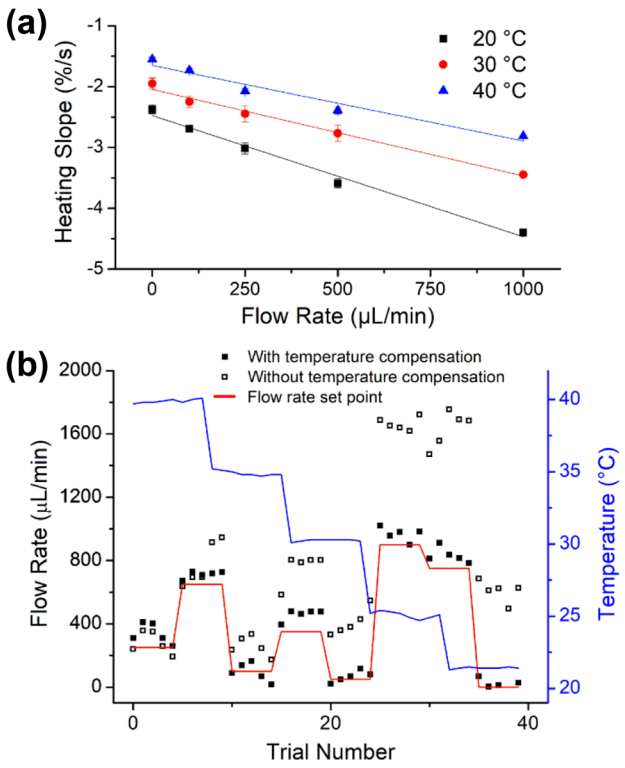

Fig. 7 **a** Flow sensor response is temperature-dependent. **b** The temperature compensation algorithm (filled squares) successfully tracked flow rate (red line) through several real-time temperature changes and resulted in a 6.6×reduction in error over data calibrated at one temperature (unfilled squares)

Each signal multiple was translated upwards as needed so that the average pressure was always equal (72 mm Hg). Distortion was faintly visible at $t = 18 - 20$ s at 1×, suggesting good in vivo IMSM performance.

Sensor standard deviation and error versus ICP amplitude were also calculated to quantify precision and accuracy, respectively (Fig. 9). IMSM-transduced flow rates for each ICP amplitude (n = 3) were compared with LD20-transduced flow rates averaged over the measurement period (240 s) to calculate error. The combined LD20 flow rate average was used to minimize the effect of variations in the physiological data set. While error appears randomly distributed in both sign and magnitude, indicating that pulsatility does not impart any systematic bias, there may be a slight positive relationship between input amplitude and flow measurement imprecision ($R^2 = 0.26$).

The flow sensor was tested using deidentified human CSF to closely simulate the in vivo environment. Calibration curves at room and body temperature using CSF and 1×PBS were not different for all but 2 measurements (Fig. 10a). Following this step, flow rate measurements in CSF flow measured hourly for 44 h in our benchtop EVD model resulted in minimal and nonmonotonic error drift (Fig. 10b). Flow was stopped at 42 h to simulate an occlusion; this event was detected by the IMSM. The experiment was halted at 44 h due to CSF evaporation and conductivity increase. For this experiment, flow was imposed on the system using a peristaltic pump (120U/DM3, Watson Marlow, Falmouth, UK) and gold standard flow measurement was provided by a commercial flow sensor (SLI-1000, Sensirion AG, ZH, Switzerland).

5.2 Temperature sensor

Using the electronics board, heater resistance was measured in 1×PBS at 5 equally spaced temperatures from 20 – 40 °C for 25 days in dry storage (3 trials, Fig. S8). We observed low variability between trials, good linearity, and

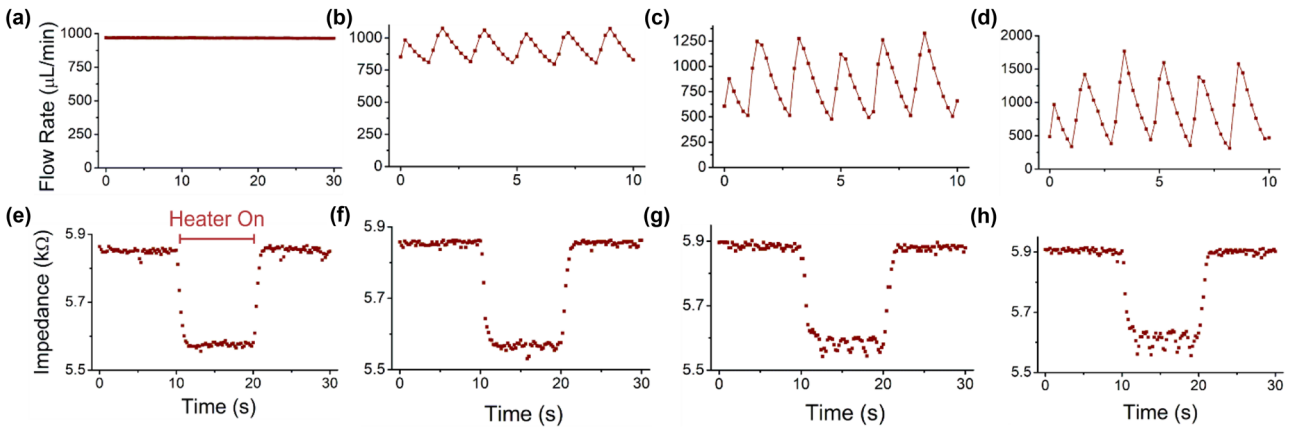

Fig. 8 Input flow rates (top) and resultant representative IMSM output flow sensor curves (bottom). **a**–**d** Representative input flow rate signals are plotted for constant pressure and 1×, 3×, and 5×the physiological sample in order to increase amplitude. **e**–**h** Representative output heating curves are presented adjacent to their corresponding inputs. Some visible distortion appears at 1×and is more visible at 3×and 5×amplitude

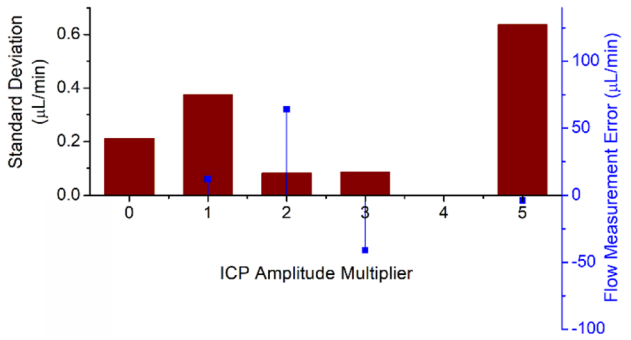

Fig. 9 The standard deviation (n = 3) of IMSM flow measurements and measurement error at each input amplitude are plotted here to determine how pulsatility affects sensor precision. Constant flow rate (zero amplitude multiplier) is included as a control. Pulsatility decreases sensor precision, but not accuracy

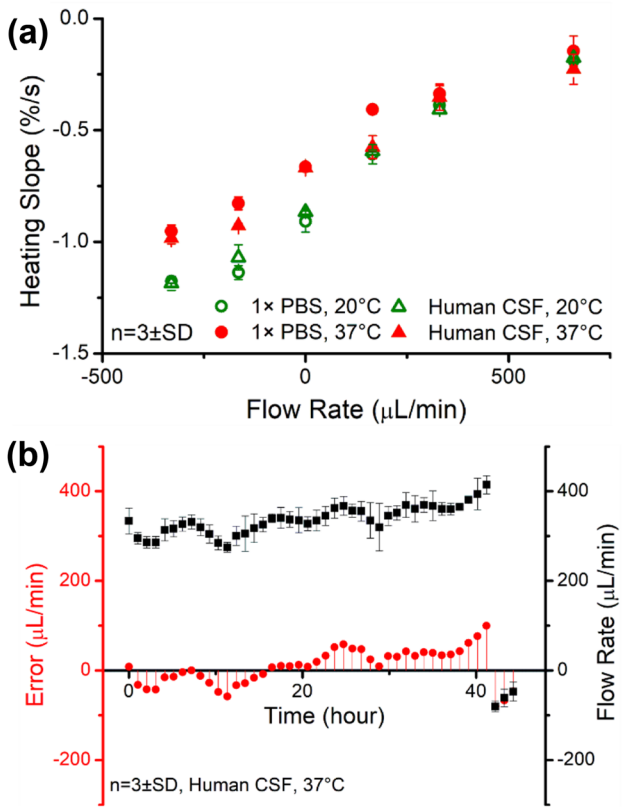

Fig. 10 **a** Device calibration in 1×PBS vs human CSF. **b** The flow sensor was tested for 44 h with human CSF. Error versus a reference flowmeter is displayed in red

no observable drift, suggesting that the sensor is stable in a saline environment such as the body for at least 25 days. Resistance was also recorded during a 10 s heating period at 4 flow rates and 3 ambient temperatures. As expected, later resistances are dependent on flow rate as the self-heating of the heater equilibrates with convective losses, while the first measurement is only dependent on ambient temperature and can be used for temperature calibration (Fig. S9).

5.3 Electrode/substrate integrity sensor

Soak testing at body temperature was performed to validate the substrate integrity sensor (covered IDEs). Two device cohorts were tested. One cohort was used as-fabricated and not subject to annealing, providing a baseline reference for adhesion failure (von Metzen and Stieglitz 2013). The other was annealed following our typical best practice process (B. J. Kim and Meng 2016). We observed a decrease in impedance with time in the unannealed but not annealed devices (Fig. 11), indicating that impedance tracks liquid intrusion into Parylene substrate. EIS recorded with the Reference 600 potentiostat corroborated these results and revealed that impedance decreased earlier and with greater magnitude at lower frequencies (Table 2) (Fig. S10).

The effect of gross electrode surface occlusion was measured by coating electrode integrity sensors (exposed IDEs) in cyanoacrylate glue. EI spectra were acquired at three occlusion states (uncoated, approximately half coated, and fully coated) using the datalogger. The states were distinguishable by characteristic shifts in the impedance magnitude plots (Fig. S11). In particular, impedance magnitude increased by approximately one order of magnitude between progressively more occluded states.

To determine the sensor response to protein adhesion, a protocol simulating EVD fluid conditions was established based on existing methodology (Pyshnov 2004). The IMSM was soaked in a 1 mg/mL BSA-FITC solution for 30 min at 20 and 40 °C to span the expected fluid temperature range. Sensors were triple rinsed in ultrapure water then imaged with fluorescence microscopy (Eclipse LV100D, Nikon, Tokyo, Japan) using a FITC filter cube. Addition of BSA-FITC at 40 °C resulted in a significant increase in fluorescence intensity ($p < 0.01$, n = 3 devices) (33 × average intensity increase) (Fig. S12). BSA-FITC adhered well to both Parylene C and platinum as observable in the post-BSA micrograph. There was no significant fluorescence increase at 20 °C, which is reasonable because BSA adhesion is promoted at higher temperatures (Pyshnov 2004). These results suggest BSA adhesion to platinum occurs within 30 min at 40 °C.

EI spectra were recorded from the exposed IDEs to determine if protein adhesion affected sensor response. Electrodes were first soaked in 1×PBS only for 30 min at 40 °C as a control (Fig. S13). There was a small, but significant difference in phase in the pre-soak (mean = −13.4°, SD = 5.4°) and post-soak conditions (mean = −18.5°, SD = 3.3°) at low frequencies (f_{test} = 20 mHz) (one-tailed, paired t-test, $p = 0.02$). There was no significant change at higher frequencies (f_{test} = 50 kHz).

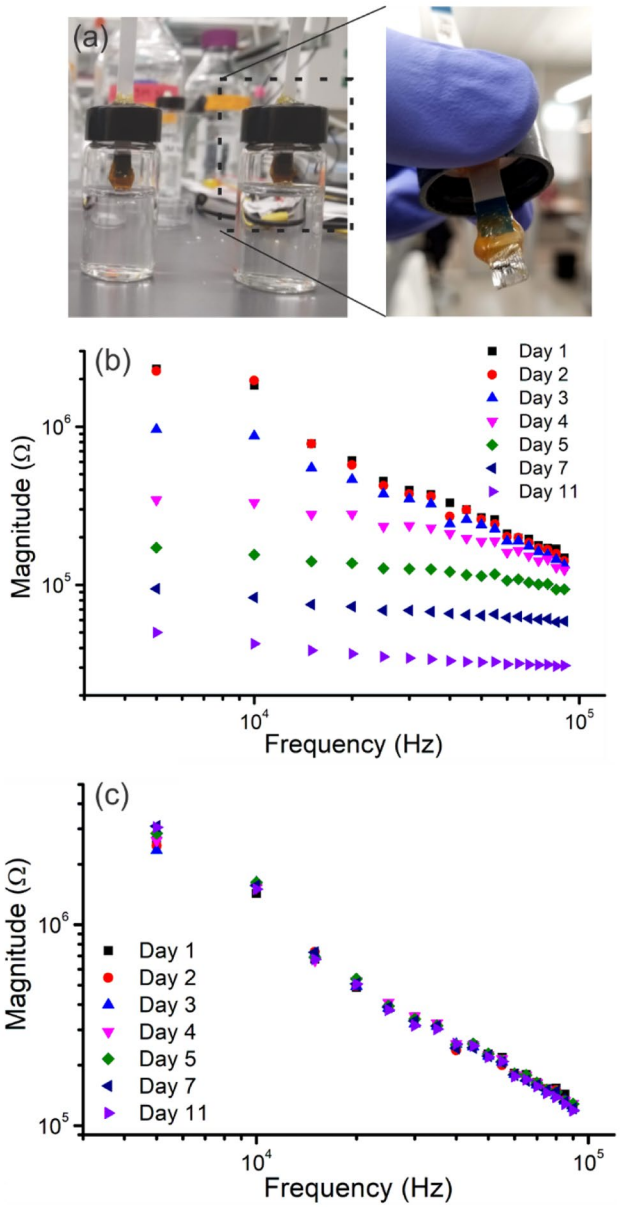

Fig. 11 **a** Photograph of soak testing vial containing sensor immersed in PBS. Inset shows cap and sensor assembly. **b** EIS magnitude of covered and unannealed IDE pair decreases with time during soak in 37 °C PBS. **c** Annealed IDE pair EIS magnitude does not change over 11 days

The experimental cohort of 4 separate electrodes were soaked in a BSA-FITC solution for 30 min at 40 °C then rinsed 3 times in ultrapure water. EIS was performed before soaking, after the BSA soak in BSA solution, and after rinsing in 1×PBS (Fig. 12). To correct for the BSA-independent phase difference observable in the control experiment at 0.02 Hz, that phase difference was subtracted from both post-soak data sets (assuming linearity). There was a significant phase response at low frequencies both in the BSA solution measurement and in the post-rinse measurement

Table 2 Sensitivity and resolution of sensors

Sensor	Sensitivity	Resolution/Standard deviation
Flow	$9.8–15\times10^{-2}$ %/μL	66–120 μL/min
Temperature	5.8 mV/°C	2 °C
Substrate	m = 89.7 MΩ/day, n = −2.27[a]	m = 69 MΩ/day, n = 0.64[a,b]
Electrode	0.15 °/AU	75 AU[c]

[a] $Z = mt^n$ where Z is impedance and t is time, at 5 kHz

[b] Standard deviation given in place of resolution

[c] 100 AU indicates BSA-FITC adhesion, based on fluorometric assay

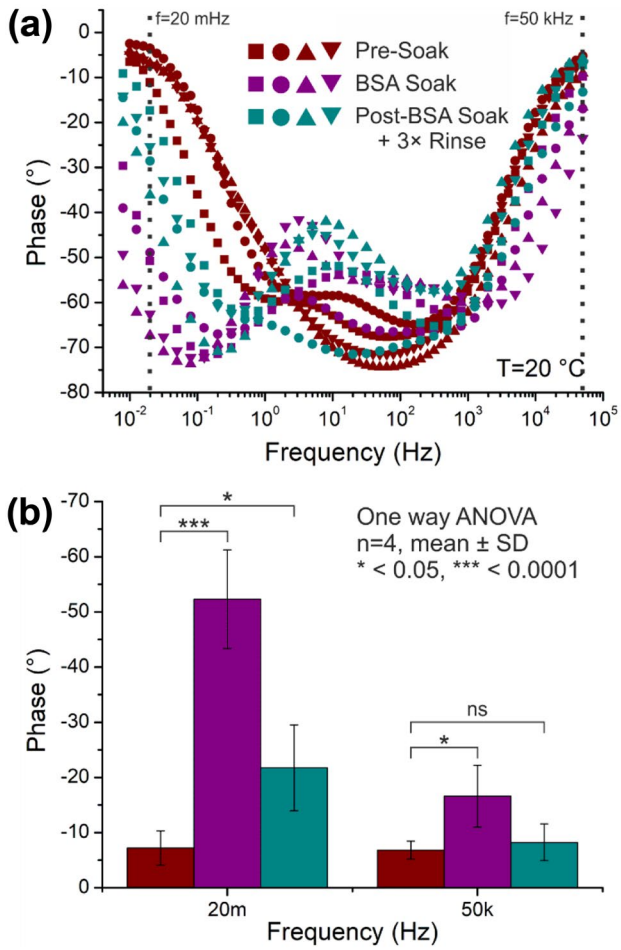

Fig. 12 **a** EI phase spectra of protein-soaked devices shows an elevated response at lower frequencies ($f = 10$ – 1000 mHz) **b** Phase response is different between the pre-BSA and post-BSA soak at 20 mHz, even after rinsing. A less significant response exists in BSA solution at 50 kHz, but not after rinsing. Asterisks represent different p values

(one-way ANOVA with Holms multiple comparisons test). There was a less significant phase response in the BSA

solution at higher frequencies, and no significant response in the post-rinse solution.

5.4 Chronic IMSM testing

IMSM sensors were tested for 53 days using PBS in our benchtop EVD model to assess sensor drift and substrate / electrode integrity over time. Two disruptive events were added to the protocol to simulate nonideal flow conditions. Ambient temperature was changed from 37 to 27 °C from day 6 – 10 (event 1), and flow was halted during day 51 to replicate occlusion (event 2).

IMSM flow rate was tracked along with data from the LD20 and Fluigent devices (Fig. 13a). Root mean square (RMS) error averaged 61.4 µL/min for the IMSM, which was sufficiently accurate to detect the zero-flow condition during event 2. There was no significant error increase during events 1 or 2. IMSM RMS error slightly increased over the experiment by 0.181 µL/min per day on average. The LD20 RMS error was 55.4 µL/min.

Events 1 and 2 are most visible in the RTD output plot (Fig. 13b). Low frequency waves may be due to room temperature fluctuations or aliasing with the ICP data set. In the raw flow sensor data (Fig. 13c), event 1 is visible though flow rate is unchanged, while the effect of event 2 is dampened due to the lower ambient temperature of the stopped flow.

EI spectra were recovered from covered (Fig. 13d) and exposed (Fig. 13e) electrodes. There was no decrease in impedance of the covered IDEs with time at the lowest frequency (5 kHz). Impedance of the exposed IDEs slowly increased over the experiment. Discontinuities at days 6–10 and 51 were due to ambient temperature decrease.

6 Discussion

Impedimetric flow sensing is a potentially transformative technology for chronic in vivo biomonitoring. RTD-based temperature compensation enables sensor use at arbitrary relevant temperatures (20–40 °C), bridging a gap between benchtop and commercial use. While impedance showed little drift over chronic experiments in this work (− 0.016%/day) and could have been used for temperature measurement itself, RTD-based methods add a level of redundancy to the system, accounting for any physiological conductivity variation for only a small increase in complexity. Lowering the heater perturbation signal during temperature measurement in a future circuit design would reduce self-heating and improve reliability. One disadvantage of temperature compensation methods is the longer time necessary for calibration experiments (~ 2 h per temperature step), which slows device preparation and increases wear. The tradeoff between compensation accuracy and calibration length can be controlled via number of temperature calibration steps.

The in vivo environment in terms of flow dynamics, temperature, and conductivity was represented by our benchtop EVD model. Importantly, the pneumatic flow controller allowed arbitrary, pulsatile pressure signals to be outputted. The physiological pressure signal was translated upwards to create appropriate flow rates (~ 330 µL/min), accounting for different fluidic resistance in the lab versus clinic. Additional features may be added to the model in future work, such as mixing blood with PBS to simulate the compromised CSF common after EVD insertion along with an analysis of horizontal versus vertical catheter placement and associated sedimentation (Harris et al. 2010; Bork et al. 2010).

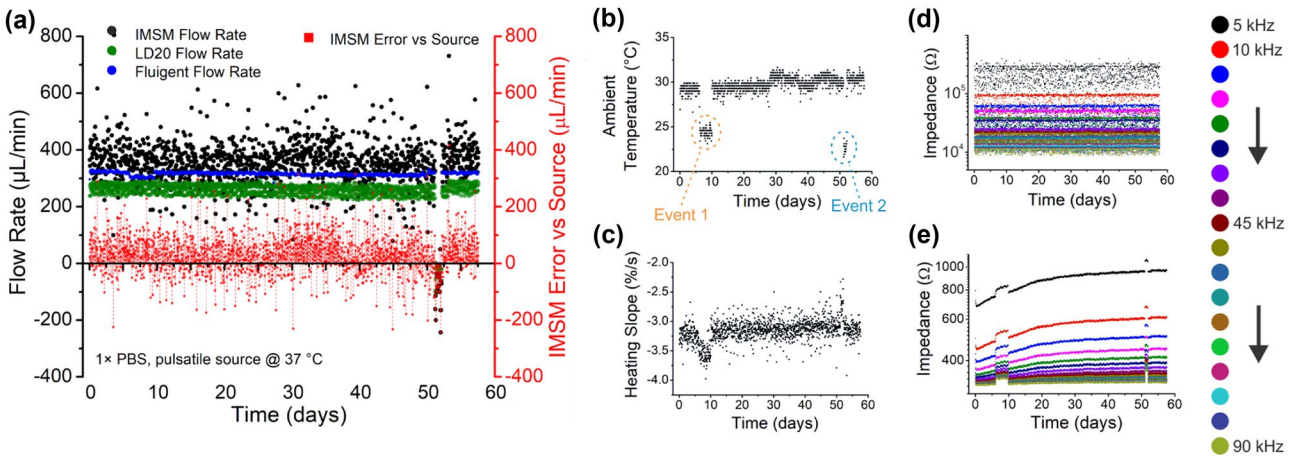

Fig. 13 **a** Chronic IMSM and LD20 flow data are presented against a benchmark. IMSM error is shown versus the benchmark on the right axis. **b** Ambient temperature transduced using the heater as an RTD. **c** Unprocessed flow sensor data with the two adverse events highlighted. **d** The covered and **e** exposed IDE responses are shown from 5 to 90 kHz as shown on the right

Table 3 CSF Flow Sensors reported in literature and industry

Paper	Sensor type	Resolution (μL/min)	Error (%)	Range (mL/hr)
Pennell et al. 2016	Off-the-shelf ultrasonic (Transonic TS420)	8.3	±15[a]	3–17.4
Madsen et al. 2020 (ShuntCheck, NeuroDX)	Trans-cutaneous thermal	Binary flow/no-flow	–	–
Qin et al. 2019	Off-the-shelf thermistor	–	±6.3[b]	0–52.5
Krishnan et al. 2018	Trans-cutaneous thermal, Cu/PI/Cu, PDMS	3 flow levels	–	0–30
This Work	Thermal impedimetric, Parylene C	48.8	±17	0–60

[a]Averaged over a 24 h recording period

[b]Post-hoc calculation using calibration curves

The similar IMSM responses between 1×PBS and human CSF suggest benchtop calibration is appropriate for in vivo use. CSF must be frozen and thawed for transport between the clinic and laboratory, which kills cells without the use of special protocols and can denature certain proteins in CSF (Klener et al. 2014). However, the cell and protein count of CSF is very low (35 mg/dL protein concentration) (Di Terlizzi and Platt 2006), and impedimetric flow sensing is robust to conductivity changes (Hudson and Meng 2021), and so we anticipate data from thawed CSF is valuable here.

Practically, testing of MEMS research devices involves risk of device failure. As part of a planned clinical study, the IMSM will be sent to a hospital and set up by clinicians who are not used to handling sensitive devices. This design restraint required robust packaging, autonomous data recording, and easy connection to clinical fluid fittings. Therefore, substrate and electrode integrity sensors were added to monitor performance, provide redundancy, and separate application-specific failures from other types. For example, a sudden increase in the impedance of all electrode pairs might indicate accidental packaging damage, while an increase of only exposed electrode impedance might suggest the presence of a bubble in the line or blood cell sedimentation in compromised CSF. Meanwhile, chronic trends can be monitored for signs of drift.

The covered IDEs showed an expected decrease in impedance with soak time as substrate liquid permeation created parasitic conduction paths between electrodes (4600% decrease in impedance from day 1 to 11), an effect shown previously (Seymour et al. 2009; Takmakov et al. 2015). To identify substrate failure earlier, the measurement board could be altered to simply record DC resistance or by adding an external clock IC to the network analyzer, extending its bandwidth. The protein response of the exposed IDEs is more ambiguous. After correcting for the phase change observed in the control soak, there is a difference in response between PBS and BSA solution at low frequencies ($p < 0.05$), which correlates with prior unpublished results (Pyshnov 2004). A smaller (though still significant) response exists after a 3×rinse. While the degree of protein adsorption after rinsing or dilution remains an open question (Vogler 2012), these results suggest BSA adhesion to platinum is at least partially reversible. It is also possible that dissolved BSA contributed to the elevated response in the pre-rinse case, though this is unlikely due to the low-frequency character of the response suggesting an interfacial effect. The comparatively weak response at the measurement frequency (50 kHz) suggests that flow sensor measurements would not be disturbed, which was corroborated in a separate experiment (Fig. S14).

Chronic IMSM flow sensor performance was acceptable. IMSM and LD20 RMS errors were nearly the same (61.4 and 55.4 μL/min), falling between the fully external ShuntCheck system which delivers a flow/no flow response only, and ultrasonic transit time flow sensors, which reported an RMS error of 10.4 μL/min in a recent study (Pennell et al. 2016) but requires bulky electronics (Table 3). The LD20 error is likely due to the source pulsatility. There was no detectable error increase during either disruptive event, demonstrating the robustness of IMSM flow transduction to real-world conditions. Similarly, the stability of the covered electrodes suggested no water intrusion occurred over 58 days in warm PBS. The shape of the impedance curve of the exposed electrodes at 5 kHz evokes a Langmuir isotherm and may result from adsorption of dissolved species onto the platinum surface, though the kinetics would be quite slow. The epoxy used was selected for its stability (Cvancara et al. 2016), however, it is possible that it generated diffusants which settled on the electrode surface. A high-powered comparative study with other candidate epoxies is needed to determine whether epoxy choice influences platinum interfacial impedance. Taken together, these chronic results suggest the IMSM is ready for use in external animal and human models.

Shunts carrying biological fluids are prone to blockage and unpredictable flow rates, which requires careful monitoring to avoid negative health impacts. Elevated ICP can cause severe neurological sequelae and even death if untreated. Quantitative and reliable CSF flow rate tracking in an EVD and eventually an implant could significantly

improve patient care and ease patient anxiety, as early symptoms of shunt failure are nonspecific, such as headache and vomiting (Khan et al. 2007). The electronics in this work were designed for EVD measurement in a hospital setting and thus relatively bulky ($9.5 \times 7.7 \times 3.0$ cm^3, 62.13 g), but sensor materials and form factor were chosen for later implantable use.

7 Conclusion

An integrated polymer-based flow, temperature, and electrode/substrate integrity sensor system was realized along with a complementary datalogger circuit. Flow sensor performance was validated in pulsatile flow and human CSF. A temperature compensation method was developed which dramatically improved performance to enable translational flow sensor measurements. The covered IDEs were found to predict substrate-based failure, which did not occur over 2 months of testing. Protein adhesion to exposed IDEs was detectable at low frequencies but did not affect flow measurements. A benchtop EVD model was designed and used for chronic testing of the IMSM, which demonstrated acceptable performance for in vivo testing.

Supplementary Information The online version contains supplementary material available at https://doi.org/10.1007/s10544-021-00579-8.

Acknowledgements The authors would like to thank Dr. Marek Czosnyka of the University of Cambridge for providing access to his clinical ICP dataset, Dr. Donghai Zhu of the USC Core Nanofabrication Facilities for his fabrication assistance and the members of the Biomedical Microsystems Lab for their helpful discussion. This work was funded in part by the National Science Foundation (NSF) under EFRI-1332394 and PFI-TT-1827773, the Rudi Schulte Research Institute, and the Coulter Translational Research Partnership Program.

References

A.A. Al-Ali, B.J. Maundy, A.S. Elwakil, *Design and Implementation of Portable Impedance Analyzers* (Springer International Publishing, Cham, Switzerland, 2019)

Al-Ali, Abdulwadood, Ahmed Elwakil, Abdelaziz Ahmad, and Brent Maundy. 2017. "Design of a Portable Low-Cost Impedance Analyzer:" In Proceedings of the 10th International Joint Conference on Biomedical Engineering Systems and Technologies, 104–9. Porto, Portugal: SCITEPRESS. https://doi.org/10.5220/0006121901040109.

D.J. Apigo, P.L. Bartholomew, T. Russell, A. Kanwal, R.C. Farrow, G.A. Thomas, An angstrom-sensitive, differential mems capacitor for monitoring the milliliter dynamics of fluids. Sens. Actuators, A **251**(November), 234–240 (2016). https://doi.org/10.1016/j.sna.2016.10.030

D.J. Apigo, P.L. Bartholomew, T. Russell, A. Kanwal, R.C. Farrow, G. Thomas, Evidence of an application of a variable MEMS capacitive sensor for detecting shunt occlusions. Sci. Rep. (2017). https://doi.org/10.1038/srep46039

A. Baldwin, Yu. Lawrence, E. Meng, An electrochemical impedance-based thermal flow sensor for physiological fluids. J. Microelectromech. Syst. **25**(6), 1015–1024 (2016). https://doi.org/10.1109/JMEMS.2016.2614664

A. Baldwin, E. Yoon, T. Hudson, E. Meng, Fluid temperature measurement in aqueous solution via electrochemical impedance. J. Microelectromech. Syst. **28**(6), 1060–1067 (2019). https://doi.org/10.1109/JMEMS.2019.2939811

D. Bigio, Biological reactions to cerebrospinal fluid shunt devices: a review of the cellular pathology. Neurosurgery **42**(2), 319–326 (1998). https://doi.org/10.1097/00006123-199802000-00064

T.L. Bonfield, E. Colton, J.M. Anderson, Plasma protein adsorbed biomedical polymers: activation of human monocytes and induction of interleukin 1. J. Biomed. Mater. Res. **23**(6), 535–548 (1989). https://doi.org/10.1002/jbm.820230602

T.L. Bonfield, E. Colton, J.M. Anderson, protein adsorption of biomedical polymers influences activated monocytes to produce fibroblast stimulating factors. J. Biomed. Mater. Res. **26**(4), 457–465 (1992). https://doi.org/10.1002/jbm.820260404

T. Bork, A. Hogg, M. Lempen, D. Müller, D. Joss, T. Bardyn, P. Büchler et al., Development and in-vitro characterization of an implantable flow sensing transducer for hydrocephalus. Biomed. Microdevice **12**(4), 607–618 (2010). https://doi.org/10.1007/s10544-010-9413-6

T.M. Clark, S.C. Malpas, D. McCormick, P. Heppner, D.M. Budgett, Implantable multi-modal sensor to improve outcomes in hydrocephalus management. IEEE Sens. J. **15**(10), 6027–6035 (2015). https://doi.org/10.1109/JSEN.2015.2451655

N.P. Cosman, S.G. Roscoe, Electrochemical quartz crystal nanobalance (EQCN) studies of protein interfacial behavior at Pt. Langmuir **20**(5), 1711–1720 (2004). https://doi.org/10.1021/la035154h

C.N. Cottonaro, H.V. Roohk, G. Shimizu, D.R. Sperling, Quantitation and characterization of competitive protein binding to polymers. ASAIO J. **27**(1), 391 (1981)

Cvancara, P., S. Lauser, L. Rudmann, and T. Stieglitz. 2016. "Investigations on Different Epoxies for Electrical Insulation of Microflex Structures." In *2016 38th Annual International Conference of the IEEE Engineering in Medicine and Biology Society (EMBC)*, 1963–66. Orlando, FL, USA: IEEE. https://doi.org/10.1109/EMBC.2016.7591108.

M. Czosnyka, J.D. Pickard, Monitoring and interpretation of intracranial pressure. J. Neurol. Neurosurg. Psychiatry **75**(6), 813–821 (2004). https://doi.org/10.1136/jnnp.2003.033126

Analog Devices. 2005. "AD5933 Data Sheet." https://www.analog.com/media/en/technical-documentation/data-sheets/AD5933.pdf.

J.M. Drake, C. Sainte-Rose, M. DaSilva, H. Jean-François, Cerebrospinal fluid flow dynamics in children with external ventricular drains. Neurosurgery **28**(2), 242–250 (1991). https://doi.org/10.1227/00006123-199102000-00011

E.T. Enikov, G. Édes, J. Skoch, R. Anton, Application of GMR sensors to liquid flow sensing. J. Microelectromech. Syst. **24**(4), 914–921 (2015). https://doi.org/10.1109/JMEMS.2014.2359174

P.A. Gardner, J. Engh, D. Atteberry, J.J. Moossy, Hemorrhage rates after external ventricular drain placement: clinical article. J. Neurosurg. **110**(5), 1021–1025 (2009). https://doi.org/10.3171/2008.9.JNS17661

Á. Giménez, M. Galarza, U. Thomale, M.U. Schuhmann, J. Valero, J.M. Amigó, Pulsatile flow in ventricular catheters for hydrocephalus. Philosophical Transact. Royal Soc. **375**(2096), 20160294 (2017). https://doi.org/10.1098/rsta.2016.0294

R. Gomez-Sjoberg, D.T. Morisette, R. Bashir, Impedance Microbiology-on-a-Chip: Microfluidic Bioprocessor for Rapid Detection of Bacterial Metabolism. J. Microelectromech. Syst. **14**(4), 829–838 (2005). https://doi.org/10.1109/JMEMS.2005.845444

W.F. Gorham, A new, general synthetic method for the preparation of linear poly-p-Xylylenes. J. Poly. Sci. **4**(12), 3027–3039 (1966). https://doi.org/10.1002/pol.1966.150041209

C.A. Gutierrez, C. Lee, B. Kim, E. Meng, 16th International Solid-State Sensors. Actuat. Microsys. Conf (2011). https://doi.org/10.1109/TRANSDUCERS.2011.5969538

H. Hämmerle, K. Kobuch, K. Kohler, W. Nisch, H. Sachs, M. Stelzle, Biostability of micro-photodiode arrays for subretinal implantation. Biomaterials **23**(3), 797–804 (2002). https://doi.org/10.1016/S0142-9612(01)00185-5

B.W. Hanak, R.H. Bonow, C.A. Harris, S.R. Browd, Cerebrospinal fluid shunting complications in children. Pediatr. Neurosurg. **52**(6), 381–400 (2017). https://doi.org/10.1159/000452840

C.A. Harris, J.H. Resau, E.A. Hudson, R.A. West, C. Moon, J.P. McAllister, Mechanical contributions to astrocyte adhesion using a novel in vitro model of catheter obstruction. Exp. Neurol. **222**(2), 204–210 (2010). https://doi.org/10.1016/j.expneurol.2009.12.027

Hudson, Trevor, Alex Baldwin, and Ellis Meng. (2019) "A Continuous, Drift-Compensated Impedimetric Thermal Flow Sensor for in Vivo Applications. In 2019 IEEE 32nd International Conference on Micro Electro Mechanical Systems (MEMS), 731–34. https://doi.org/10.1109/MEMSYS.2019.8870746.

T. Hudson, E. Meng, A continuous, impedimetric parylene flow sensor. J. Microelectromechan. Syst. **30**, 456–471 (2021)

C. Kadowaki, M. Hara, M. Numoto, K. Takeuchi, I. Saito, CSF shunt physics: factors influencing inshunt CSF flow. Child's Nervous System **11**(4), 203–206 (1995). https://doi.org/10.1007/BF00277654

A.A. Khan, A. Jabbar, A. Banerjee, G. Hinchley, Cerebrospinal shunt malfunction recognition and emergency management. British J. Hospital Med. **68**(12), 651–655 (2007). https://doi.org/10.12968/hmed.2007.68.12.651

B.J. Kim, E. Meng, Micromachining of Parylene C for BioMEMS. Polym. Adv. Technol. **27**(5), 564–576 (2016). https://doi.org/10.1002/pat.3729

S. Kim, Yu. Guiduk, T. Kim, K. Shin, J. Yoon, Rapid bacterial detection with an interdigitated array electrode by electrochemical impedance spectroscopy. Electrochim. Acta **82**, 126–131 (2012). https://doi.org/10.1016/j.electacta.2012.05.131

B.J. Kim, W. Jin, A. Baldwin, Yu. Lawrence, E. Christian, M.D. Krieger, J. Gordon McComb, E. Meng, Parylene MEMS patency sensor for assessment of hydrocephalus shunt obstruction. Biomed. Microdevice **18**(5), 87 (2016). https://doi.org/10.1007/s10544-016-0112-9

A.R. Kirmani, A.H. Sarmast, A.R. Bhat, *"Role of External Ventricular Drainage in the Management of Intraventricular Hemorrhage* (surgical neurology international, Its Complications and Management, 2015). https://doi.org/10.4103/2152-7806.172533

J. Klener, K. Hofbauerová, A. Bartoš, J. Říčný, D. Řípová, V. Kopecký, Instability of cerebrospinal fluid after delayed storage and repeated freezing: a holistic study by drop coating deposition raman spectroscopy. Clinic. Chem. Lab. Med. (CCLM) **52**(5), 657–664 (2014). https://doi.org/10.1515/cclm-2013-0800

S. Krause, M. Hahne, M. Walter, S. Kiefer, K.R. Linke, S. Leonhardt, Brain Pressure Dynamics and Control with an External Ventricular Drainage In 5th European Conference of the International Federation for Medical and Biological Engineering, edited by Ákos Jobbágy. Berlin Heidelberg Berlin, Heidelberg (2011). https://doi.org/10.1007/978-3-642-23508-5_82

S.R. Krishnan, T.R. Ray, A.B. Ayer, Y. Ma, P. Gutruf, KunHyuck Lee, J.Y. Lee et al., Epidermal electronics for noninvasive, wireless, quantitative assessment of ventricular shunt function in patients with hydrocephalus. Sci. Translat. Med. **10**(465), 8437 (2018). https://doi.org/10.1126/scitranslmed.aat8437

P. Lackner, R. Beer, G. Broessner, R. Helbok, K. Galiano, C. Pleifer, B. Pfausler et al., Efficacy of silver nanoparticles-impregnated external ventricular drain catheters in patients with acute occlusive hydrocephalus. Neurocrit. Care **8**(3), 360–365 (2008). https://doi.org/10.1007/s12028-008-9071-1

D.D. Limbrick, S. Lake, M. Talcott, B. Alexander, S. Wight, J.T. Willie, W.D. Richard, G.M. Genin, E.C. Leuthardt, The baric probe: a novel long-term implantable intracranial pressure monitor with ultrasound-based interrogation: technical note. J. Neurosurg. Pediatr. **10**(6), 518–524 (2012). https://doi.org/10.3171/2012.8.PEDS11565

A.A. Linninger, M. Xenos, D.C. Zhu, M.R. Somayaji, S. Kondapalli, R.D. Penn, Cerebrospinal fluid flow in the normal and hydrocephalic human brain. IEEE Trans. Biomed. Eng. **54**(2), 291–302 (2007). https://doi.org/10.1109/TBME.2006.886853

B.R. Lutz, P. Venkataraman, S.R. Browd, New and improved ways to treat hydrocephalus: pursuit of a smart shunt. Surg. Neurol. Int. **4**(1), S38-50 (2013). https://doi.org/10.4103/2152-7806.109197

J.R. Madsen, T.P. Boyle, M.I. Neuman, E.-H. Park, M.S. Tamber, R.W. Hickey, G.G. Heuer et al., Diagnostic accuracy of non-invasive thermal evaluation of ventriculoperitoneal shunt flow in shunt malfunction: a prospective, multi-site, operator-blinded study. Neurosurgery **87**(5), 939–948 (2020). https://doi.org/10.1093/neuros/nyaa128

E. Meng, P.-Y. Li, Y.-C. Tai, Plasma removal of parylene C. J. Micromech. Microeng. **18**(4), 045004 (2008). https://doi.org/10.1088/0960-1317/18/4/045004

R.P. Metzen, von, and Thomas Stieglitz. , The effects of annealing on mechanical, chemical, and physical properties and structural stability of parylene C. Biomed. Microdevice **15**(5), 727–735 (2013). https://doi.org/10.1007/s10544-013-9758-8

B.J.E. Misgeld, I.M. Elixmann, L. Fahnster, M. Walter, M. Weinzierl, W. Steudel, S. Leonhardt, Design and evaluation of an automatic extraventricular drainage control system. IEEE Trans. Control Syst. Technol. **23**(6), 2283–2292 (2015). https://doi.org/10.1109/TCST.2015.2413377

P. Moshayedi, G. Ng, J.C.F. Kwok, G.S.H. Yeo, C.E. Bryant, J.W. Fawcett, K. Franze, J. Guck, The relationship between glial cell mechanosensitivity and foreign body reactions in the central nervous system. Biomaterials **35**(13), 3919–3925 (2014). https://doi.org/10.1016/j.biomaterials.2014.01.038

R. Muralidharan, External ventricular drains: management and complications. Surg. Neurol. Int. **6**(6), S271–S274 (2015). https://doi.org/10.4103/2152-7806.157620

Nordbotten, Bernt Jørgen. 2008. "Bioimpedance Measurements Using the Integrated Circuit AD5933." M.S. Thesis, University of Oslo.

S. Omanovic, S.G. Roscoe, Electrochemical studies of the adsorption behavior of bovine serum albumin on stainless steel. Langmuir **15**(23), 8315–8321 (1999). https://doi.org/10.1021/la990474f

J. Ortigoza-Diaz, K. Scholten, E. Meng, Characterization and modification of adhesion in dry and wet environments in thin-film parylene systems. J. Microelectromech. Syst. **27**(5), 874–885 (2018). https://doi.org/10.1109/JMEMS.2018.2854636

T. Pennell, J.L. Yi, B.A. Kaufman, S. Krishnamurthy, Noninvasive measurement of cerebrospinal fluid flow using an ultrasonic transit time flow sensor: a preliminary study. J. Neurosurg. Pediatr. **17**(3), 270–277 (2016). https://doi.org/10.3171/2015.7.PEDS1577

C.P. Pennisi, C. Sevcencu, A. Dolatshahi-Pirouz, M. Foss, J. Lundsgaard Hansen, A. Nylandsted Larsen, V. Zachar, F. Besenbacher, K. Yoshida, Responses of fibroblasts and glial cells to nanostructured platinum surfaces. Nanotechnology **20**(38), 385103 (2009). https://doi.org/10.1088/0957-4484/20/38/385103

R.K.R. Phillips, S. Omanovic, S.G. Roscoe, Electrochemical studies of the effect of temperature on the adsorption of yeast alcohol dehydrogenase at Pt. Langmuir **17**(8), 2471–2477 (2001). https://doi.org/10.1021/la0007729

J. Prusseit, M. Simon, C. von der Brelie, A. Heep, E. Molitor, S. Völz, A. Simon, Epidemiology, prevention and management of

ventriculoperitoneal shunt infections in children. Pediatr. Neurosurg. **45**(5), 325–336 (2009). https://doi.org/10.1159/000257520

E. Pyshnov, *Electrochemical Studies of the Adsorption of Bovine Serum Albumin on a Platinum Surface* (Thesis, McGill University, M.E, 2004)

C. Qin, A.H. Olivencia-Yurvati, A.G. Williams, D. Eskildsen, R.T. Mallet, P.K. Dasgupta, Inline flow sensor for ventriculoperitoneal shunts: experimental evaluation in swine. Med. Eng. Phys. **67**(May), 66–72 (2019). https://doi.org/10.1016/j.medengphy.2019.03.010

R. Raj, S. Lakshmanan, D. Apigo, A. Kanwal, S. Liu, T. Russell, J.R. Madsen, G.A. Thomas, R.C. Farrow, "Demonstration that a new flow sensor can operate in the clinical range for cerebrospinal fluid flow." Sens. Actuators, A **234**, 223–231 (2015). https://doi.org/10.1016/j.sna.2015.08.023

S. Rammos, J. Klopfenstein, L. Augsburger, H. Wang, A. Wagenbach, J. Poston, G. Lanzino, Conversion of external ventricular drains to ventriculoperitoneal shunts after aneurysmal subarachnoid hemorrhage: effects of site and protein/red blood cell counts on shunt infection and malfunction: clinical article. J. Neurosurg. **109**(6), 1001–1004 (2008). https://doi.org/10.3171/JNS.2008.109.12.1001

Rasalingam, Vinnothini. 2018. "A System for Electrochemical Impedance Spectroscopy of Electorchemical Sensors." M.S. Thesis, Imperial College London.

D. Rodger, A. Fong, W. Li, H. Ameri, A. Ahuja, C. Gutierrez, I. Lavrov, H. Zhong, P. Menon, E. Meng, Flexible parylene-based multielectrode array technology for high-density neural stimulation and recording. Sens. Actuators, B Chem. **132**(2), 449–460 (2008). https://doi.org/10.1016/j.snb.2007.10.069

B.Z. Roitberg, N. Khan, M.S. Alp, T. Hersonskey, F.T. Charbel, J.I. Ausman, Bedside external ventricular drain placement for the treatment of acute hydrocephalus. British J Neurosur **15**, 324–327 (2001)

R. Rouhana, S.M. Budge, S.M. MacDonald, S.G. Roscoe, Electrochemical studies of the interfacial behaviour of a-lactalbumin and bovine serum albumin. Food Res. Int. **30**(1), 13–20 (1997)

K. Scholten, E. Meng, Materials for microfabricated implantable devices: a review. Lab Chip **15**(22), 4256–4272 (2015). https://doi.org/10.1039/C5LC00809C

J.P. Seymour, Y.M. Elkasabi, H.-Y. Chen, J. Lahann, D.R. Kipke, The insulation performance of reactive parylene films in implantable electronic devices. Biomaterials **30**(31), 6158–6167 (2009). https://doi.org/10.1016/j.biomaterials.2009.07.061

P. Takmakov, K. Kiersten Ruda, S. Phillips, I.S. Isayeva, V. Krauthamer, C.G. Welle, Rapid evaluation of the durability of cortical neural implants using accelerated aging with reactive oxygen species. J. Neural Eng. **12**(2), 026003 (2015). https://doi.org/10.1088/1741-2560/12/2/026003

Di. Terlizzi, Roberta, and Simon Platt. , The function, composition and analysis of cerebrospinal fluid in companion animals: part i - function and composition. Vet. J. **172**(3), 422–431 (2006). https://doi.org/10.1016/j.tvjl.2005.07.021

M. Turgut, D. Alabaz, F. Erbey, E. Kocabas, T. Erman, E. Alhan, N. Aksaray, Cerebrospinal fluid shunt infections in children. Pediatr. Neurosurg. **41**(3), 131–136 (2005). https://doi.org/10.1159/000085869

N. Turner, M. Armitage, R. Butler, G. Ireland, An in vitro model to evaluate cell adhesion to metals used in implantation shows significant differences between palladium and gold or platinum. Cell Biol. Int. **28**(7), 541–547 (2004). https://doi.org/10.1016/j.cellbi.2004.04.009

E.A. Vogler, Protein adsorption in three dimensions. Biomaterials **33**(5), 1201–1237 (2012). https://doi.org/10.1016/j.biomaterials.2011.10.059

A. Wang, X. Liang, J.P. McAllister II, J. Li, K. Brabant, C. Black, P. Finlayson et al., Stability of and inflammatory response to silicon coated with a fluoroalkyl self-assembled monolayer in the central nervous system. J. Biomed. Mater. Res., Part A **81A**(2), 363–372 (2007). https://doi.org/10.1002/jbm.a.31034

P. Webb, Temperatures of skin, subcutaneous tissue, muscle and core in resting men in cold, comfortable and hot conditions. Eur. J. Appl. Physiol. **64**(5), 471–476 (1992). https://doi.org/10.1007/BF00625070

J.E.I. Wright, K. Fatih, C.L. Brosseau, S. Omanovic, S.G. Roscoe, L-Phenylalanine adsorption on pt: electrochemical impedance spectroscopy and quartz crystal nanobalance studies. J. Electroanal. Chem. **550–551**, 41–51 (2003). https://doi.org/10.1016/S0022-0728(03)00026-3

L. Yang, Y. Li, Detection of viable salmonella using microelectrode-based capacitance measurement coupled with immunomagnetic separation. J. Microbiol. Methods **64**(1), 9–16 (2006). https://doi.org/10.1016/j.mimet.2005.04.022